CHEMISTRY OF MATERIALS

ARTICLE

pubs.acs.org/cm

Multiconstituent Synthesis of $LiFePO_4$/C Composites with Hierarchical Porosity as Cathode Materials for Lithium Ion Batteries

Anh Vu and Andreas Stein*

Department of Chemistry, University of Minnesota, 207 Pleasant St. SE., Minneapolis, Minnesota 55455, United States

Supporting Information

ABSTRACT: Monolithic, three-dimensionally ordered macroporous and meso-/microporous (3DOM/m) $LiFePO_4$/C composite cathodes for lithium ion batteries were synthesized by a multiconstituent, dual templating method. Precursors containing sources for lithium, iron, and phosphate, as well as a phenol-formaldehyde sol and a nonionic surfactant were infiltrated into a colloidal crystal template. Millimeter-sized monolithic composite pieces were obtained, in which $LiFePO_4$ was dispersed in a carbon phase around an interconnected network of ordered macropores. The composite walls themselves contained micropores or small mesopores. The carbon phase enhanced the electrical conductivity of the cathode and maintained $LiFePO_4$ as a highly dispersed phase during the synthesis and during electrochemical cycling. Monoliths containing 30 wt % C were electrochemically cycled in a 3-electrode cell with lithium foil as counter and reference electrodes. No additional binder or conductive agent was used. The capacity was as high as 150 mA h g^{-1} at a rate of C/5, 123 mA h g^{-1} at C, 78 mA h g^{-1} at 8C, and 64 mA h g^{-1} at 16C, showing no capacity fading over 100 cycles. In spite of the low electronic conductivity of bulk $LiFePO_4$ (10^{-9}–10^{-10} S cm^{-1}), the monolithic $LiFePO_4$/C composite was able to support current densities as high as 2720 mA g^{-1}.

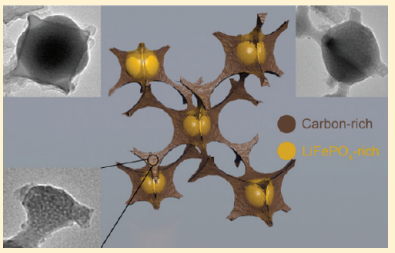

KEYWORDS: lithium iron phosphate, carbon, composites, cathode, lithium ion battery, porous electrodes

INTRODUCTION

In recent years, much research on cathode materials for lithium ion batteries has focused on $LiFePO_4$, because it has several advantageous features for large volume energy storage applications, for example, in electric vehicles (EVs) and hybrid electric vehicles (HEVs).[1] Currently, most lithium ion batteries designed for portable devices use cathodes based on $LiCoO_2$, but this material is relatively expensive and toxic compared to several alternative cathode materials and presents safety concerns when the electrode is overcharged, especially at high temperatures.[2,3] Overcharging causes the collapse of the $LiCoO_2$ structure, which is accompanied by evolution of oxygen and the potential for an explosion.[4,5] These drawbacks can be mitigated to some degree by using mixed metal oxides ($LiNi_xCo_{1-x}O_2$ and $LiMn_xNi_yCo_{1-x-y}O_2$), but the high cost and environmental effects of Co-based cathodes remain unavoidable. Unlike $LiCoO_2$, olivine $LiFePO_4$ and other phosphate-based cathodes have strong P–O covalent bonds, which stabilize the structure, preventing abrupt oxygen evolution.[1] Because of the relative abundance of iron ores, iron-based cathodes are less costly than Co-containing electrodes. Furthermore, olivine $LiFePO_4$ has a reasonably high theoretical capacity (170 mA h g^{-1}) with almost no capacity fading even after a few hundred cycles. However, the low electronic conductivity (10^{-9} to 10^{-10} S cm^{-1}),[6] and slow one-dimensional lithium diffusion limit the high rate performance of olivine $LiFePO_4$.

To overcome the low electronic conductivity, $LiFePO_4$ particles are usually coated with conductive agents (carbon, polymers, RuO_2, or others) or doped with supervalent cations.[7−9] Chung et al. found that the conductivity of olivine $LiFePO_4$ doped with Mg^{2+}, Al^{3+}, Ti^{4+}, Zr^{4+}, Nb^{5+}, or W^{6+} was improved by up to 8 orders of magnitude.[6] Recently, Kang and Ceder synthesized nanosized $LiFePO_4$ coated with a thin layer of lithium phosphate, which acted as a Li^+ reservoir to direct Li^+ into the *b* and *c* directions of the unit cell, enhancing the diffusion of Li^+ in the particles.[8] This cathode construction could be cycled at rates as high as 400C (i.e., charged and recharged within a few seconds), which would be sufficient for EV and HEV applications. However, it has still not been resolved whether the high rate performance was due to carbon residues from an organic source or due to the formation of other conductive phases, such as FeP, Fe_2P. Huang et al.[10] prepared a $LiFePO_4$/C composite by mixing a $LiFePO_4$ precursor with a carbon gel, which inhibited the growth of $LiFePO_4$ particles when treated at high temperature and acted as an electronic conductive matrix in the final composite, giving the material high capacity and good life cycles (158 mA h g^{-1} at C/5 and 120 mA h g^{-1} at 5C rate). Konarova et al.[11] prepared $LiFePO_4$/C composites with different amounts of carbon by ultrasonic spray pyrolysis followed by heat treatment and found that with 1.87 wt % of carbon, the composite exhibited capacities of 140 mA h g^{-1} at C/10 and 84 mA h g^{-1} at 5C.

The slow lithium diffusion can be addressed by decreasing particle dimensions to the nanometer scale to reduce diffusion paths.[12−14] However, the surface chemistry of nanoparticles is

Received: April 26, 2011
Revised: May 25, 2011
Published: June 16, 2011

more complex than that of their micrometer-sized analogues, and factors such as the interconnectivity of particles, formation of a solid electrolyte interphase (SEI) layer, nucleation and aggregation of particles during cycling strongly affect the performance of the electrode. Gaberscek et al.[15] reported that at a lower rate (<1C), the rate-limiting step depended on active particle sizes, while at higher rates, the rate-determining step depended on how the particles were wired. Therefore, a method to synthesize well-wired $LiFePO_4$ nanoparticles would be interesting for high rate batteries.

Porous materials have been investigated as electrode materials for high rate lithium ion batteries due to their nanometer-sized features and high surface areas, which increase the ion-exchange rates between electrolyte and active material.[16−22] To-date, much of the work on porous electrodes, particularly mesoporous ones, has focused on anode materials such as C, Sn, SnO_2, TiO_2, and their composites, the mesostructures of which are fairly well understood, and which have found applications in various fields including catalysis, separation, and adsorption.[19,22−27] In contrast, work on mesoporous cathodes, mostly metal oxides and metal phosphates, has been more limited until recently. The main reason for this is that the electrochemical performance of cathodes tends to be better when these are highly crystalline; higher crystallinity requires higher temperature syntheses, which tend to produce large grains that are incompatible with maintaining ordered mesopore structures.[28−30]

Driven by the needs of the HEV market, a few recent studies have addressed porous cathodes, including cathodes with hierarchical porosity.[15,31−33] Doherty et al.[34,35] prepared macroporous and mesoporous $LiFePO_4$ using poly(methyl methacrylate) (PMMA) colloidal crystal and surfactant templates, which showed that the rate performance of mesoporous $LiFePO_4$ is better than that of macroporous $LiFePO_4$, confirming the importance of a high surface area for improving rate capability. High surface area $LiFePO_4$ could also be obtained by using a mesoporous support. Wang et al.[36] prepared $LiFePO_4$/C composites based on the mesoporous carbon CMK-13, while Doherty et al.[37] prepared $LiFePO_4$ inside hierarchically porous carbon synthesized from a porous silica template. They obtained materials with capacities as high as 118 mA h g^{-1} at 10C for the material built around the CMK-13 support and 124 mA h g^{-1} at 5C when the hierarchical carbon support was used. However, these approaches required separate synthesis steps for the formation of the carbon host and the $LiFePO_4$/carbon composite phase and careful control during infiltration of the inorganic precursor to ensure high loadings of the active phase.

Here we synthesized $LiFePO_4$/carbon composites with hierarchical porosity by a multiconstituent synthesis,[38,39] in which all components (precursors for carbon and $LiFePO_4$ together with surfactant templates) were infiltrated into a colloidal crystal template together. Additional heat treatment was applied to improve the cross-linking and polymerization of the precursor so that a robust, interconnected framework was formed that surrounded the colloidal spheres. Slow ramping rates and multistep temperature programs were used to transform the precursor into a solid and remove the template. This procedure yielded an inverse opal or three dimensionally ordered macroporous and meso-/microporous (3DOM/m)[40] structure of the target materials. For colloidal spheres with 400−500 nm diameters, structures were typically characterized by 300−400 nm pores connected by 50−100 nm windows and 20−50 nm thick walls. The surfactant templates were intended to introduce additional mesopores into the walls. The built-in carbon phase was intimately mixed with the electrochemically active $LiFePO_4$ phase, effectively wiring $LiFePO_4$ particles together in a long-range ordered network. In this configuration, carbon bridges enhanced the conductivity of the system and helped to maintain the porous structure during cycling. Compared to conventional coating methods, in which micrometer-sized $LiFePO_4$ particles are covered with thin layers of carbon, the connectivity in the 3DOM/m $LiFePO_4$/C composite materials is better defined, surface areas are larger, and particle sizes of the cathode phase are smaller. Therefore less polarization and improved rate performance are expected.

EXPERIMENTAL SECTION

Materials. The chemicals used in this study were obtained from the following sources: methyl methacrylate (MMA) monomer (99%), 2,2′-azobis(2-methyl propionamidine) dihydrochloride (AMPD) initiator (97%), concentrated aqueous H_3PO_4 solution (85 wt %) from Aldrich; lithium perchlorate (99.0%), ethylene carbonate (>99.0%), dimethyl carbonate (>99.0%) from Fluka; $FeCl_2 \cdot 4H_2O$ (98%), LiCl (99.5%), phenol (ACS reagent), and formaldehyde solution (37% aqueous solution) from Fisher Scientific; Pluronic F127 from BASF; hydrochloric acid (37%) from Mallinckrodt Chemicals; and sodium carbonate (anhydrous, 99.7%) from J.T. Baker. Deionized water was purified to a resistance higher than 18 MΩ.

Poly(phenol formaldehyde) (PF) Sol Preparation. Prepolymerized PF sol was prepared following an established method.[41] Briefly, phenol (61 g) was melted at 50 °C in a 500 mL round-bottom flask using an oil bath. Under constant stirring, 13.6 g of NaOH aqueous solution (20 wt %) was added slowly to the melted liquid over a period of 15 min. After that, 110.4 g of aqueous formaldehyde solution (37 wt %) was added dropwise into the mixture. The solution was stirred at 500 rpm and heated at 70 °C for 1 h to increase the polymerization rate. The product was neutralized with 0.6 M HCl, filtered to remove NaCl, and water was removed by vacuum evaporation at 50 °C overnight. The dried product was dissolved in 80 g of ethanol to obtain the PF-sol, which was stored under refrigeration.

PMMA Sphere Synthesis and Assembly of Colloidal Crystal. Polymeric colloidal crystal templates composed of 400 ± 10 nm diameter PMMA spheres were synthesized using an emulsifier-free emulsion polymerization.[42] MMA monomer (400 mL) and deionized water (1600 mL) were added to a 3 L five-neck, round-bottom flask. The monomer solution was heated to 70 °C before the addition of initiator. During heating, the solution was stirred and purged with nitrogen gas. When the temperature fluctuation was less than 0.2 °C, 1.50 g of the initiator, 2,2′-azobis(2-methylpropionamidine) dihydrochloride, dissolved in 25 mL of deionized water was added to the flask. The solution turned milky white as MMA began to polymerize, forming a colloidal suspension. When the reaction had finished, the milky solution was filtered through glass wool to remove large agglomerates from the monodisperse sphere suspension. Subsequently, the PMMA sphere suspension was poured into a crystallization dish and was allowed to sediment. Opalescent PMMA colloidal crystals were obtained after the spheres settled and water was removed. The material was then broken with a spatula into small pieces, and pieces with an approximate size of $1 \times 1 \times 0.4$ cm^3 were used as the templates. PMMA sphere sizes were determined from scanning electron microscopy (SEM) images of the colloidal crystals, taking averages and standard deviations over about 200 spheres.

3DOM/m $LiFePO_4$ Preparation. 3DOM/m $LiFePO_4$/C composites were prepared by a dual templating method, in which the nonionic surfactant F127 (the poly(ethylene oxide)-poly(propylene oxide)-poly(ethylene oxide) triblock copolymer $PEO_{106}PPO_{70}PEO_{106}$) and

PMMA colloidal crystals were intended as templates for mesopores and macropores, respectively. All syntheses were carried out according to the following procedure: PF-sol (2 g) was mixed with 2 g of aqueous HCl (0.2 M) in a 20 mL vial and stirred for 15 min. F127 surfactant (1 g) was then added and stirred until a clear solution was obtained. $FeCl_2$ (1.988 g) and LiCl (0.435 g) were mixed and ground in a mortar, then transferred to the solution. At this point, the color of the solution changed from light yellow to green. The vial was placed in a larger glass bottle under flowing nitrogen to avoid the oxidation of Fe^{2+}. The mixture was vigorously stirred until all the salts were dissolved (usually 3−4 h, add 0.5 mL of ethanol if the solution is too viscous), then concentrated H_3PO_4 (0.011 mol) was slowly added to the solution, and the mixture was stirred overnight. The order of addition of each component was crucial to maintain a clear, homogeneous precursor solution before and during infiltration into the PMMA templates. In addition, the F127 surfactant was required to prevent immediate complexation of Fe^{2+} with phenol groups in the PF-sol, which prevented penetration of the colloidal templates. With F127, the precursor was stable as a homogeneous solution for 24 h in air and up to 48 h in a nitrogen atmosphere. For template infiltration, several pieces of PMMA colloidal crystal templates were placed upright in a 20 mL vial, and the precursor solution was slowly added until the template pieces were partially immersed. The templates were infiltrated as a result of capillary forces. After 4 h, the infiltrated pieces were removed from the solution, gently touched with KimWipes paper tissue to wick away excess liquid, and then placed in a vacuum chamber for 30 min at room temperature. A second infiltration step was carried out following the same procedure. The samples were then placed in a vial that had been purged with nitrogen. The sealed vial was heated at 100 °C for 24 h, then at 140 °C for 24 h to increase the amount of cross-linking and to strengthen the composite. The aged composite samples were polished with 600-grit sand paper to remove nontemplated $LiFePO_4$ from the surface before pyrolysis. 3DOM/m $LiFePO_4$/C composites were obtained by pyrolyzing the thermally cured composite under flowing N_2 (0.8 L min^{-1}) at 350 °C for 5 h and then at 600, 700, or 800 °C for another 10 h with a heating rate of 1 °C min^{-1}.

Product Characterization. All samples were ground into fine powder before structural analyses. Product crystallinities and phase purities were determined by powder X-ray diffraction (XRD) using a PANalytical X-Pert PRO MPD X-ray diffractometer equipped with a cobalt source and an X-Celerator detector. Data were collected from 10° to 85° 2θ, at a step size of 0.017° and a rate of 20.7 s/step. Average crystallite sizes were estimated by Rietveld refinement using X'pert HighScore Plus 2.0a software. Instrumental broadening was corrected using a LaB_6 standard. Small-angle X-ray scattering (SAXS) data were acquired on a Rigaku RU-200BVH 2D SAXS instrument using a 12 kW-rotating anode with a Cu source and a Siemens Hi-Star multiwire area detector. Raman spectroscopy was performed with a Witec Alpha300R confocal Raman microscope using 514.5 nm incident radiation at the lowest possible potential to minimize beam damage of the sample. Scanning electron microscopy (SEM) was carried out with a JEOL-6700 microscope operating at 5 kV with emission currents ranging from 2 to 10 μA. Transmission electron microscopy (TEM) was carried out with a Technai T12 microscope operating at 120 kV with emission currents ranging from 7 to 12 μA. Thermogravimetric (TG) analysis and differential scanning calorimetry (DSC) were performed on a Netzsch model STA 409 instrument to determine a suitable temperature program for the precursor transformation (flowing nitrogen atmosphere) and to determine the carbon content in the final products (flowing air atmosphere), using a heating rate of 5 °C min^{-1} to a final temperature of 900 °C. Nitrogen-sorption measurements were performed on a Micromeritics ASAP 2000 gas sorptometer. Samples were degassed to 0.003 mmHg for 12 h at 60 °C. Specific surface areas were calculated by the Brunauer−Emmett−Teller (BET) method, and pore sizes and volumes were estimated from pore size distribution curves from the adsorption branches of the isotherms.

Electrochemical Tests. All electrochemical tests were carried out using an Arbin battery-testing system (ABTS 4.0). Galvanostatic charge−discharge measurements were performed with a three-electrode cell, in which a 3DOM/m $LiFePO_4$/C monolith was used as the working electrode, and Li metal as the counter and reference electrodes. The cell was constructed by sandwiching a monolithic $LiFePO_4$/C sample and lithium foil separated by two Celgard films between two glass slides. The cell was then placed in a three-neck, round-bottom glass flask containing an electrolyte solution composed of 1.0 M $LiClO_4$ in a mixture of ethylene carbonate and dimethyl carbonate (1:1 vol:vol). The cell was constructed in a dry room with <1% relative humidity. For cycling experiments, constant currents were applied, and the voltages were restricted to a window of 2.0−4.2 V with 5 min rest periods between each step. All potential values are reported versus Li/Li^+, and specific capacities are reported per gram of $LiFePO_4$.

The electronic conductivity of the composites was measured at room temperature via the 4-probe van der Pauw method using a Solartron SI 1287 electrochemical interface.[43] The samples were connected to copper wires at four points A, B, C, D using silver paste. Constant currents were applied through two points A and B, while voltages were measured between two points C and D. The samples were then rotated to apply current through B and C and measure voltages between A and D. Two sets of data were linearly fitted to calculate R_{ABCD} and R_{BCAD}, which were used to calculate conductivity through the van der Pauw equation.

RESULTS AND DISCUSSION

For high rate batteries, crystalline cathode materials are preferred to provide fast ionic transport.[44] However, in surfactant-templated syntheses, extensive crystallization is usually deleterious to the mesostructure. An ideal high-rate cathode material would have a structure with interconnected pores and thin crystalline walls of active material, which can be obtained by adding supporting agents (e.g., C, Si) and by controlling crystallization.[45,46] Suitable additives for mesoporous cathode materials should be able to strengthen the mesostructure and also be electronically conductive to enhance the rate performance of the electrodes. In this work, polymer-derived carbon was selected as an integral component in the composite cathode because it can readily form mesoporous structures and has good electrical conductivity.

TG-DSC analysis of the thermally cured PMMA/precursor composite was carried out under a nitrogen atmosphere to find a suitable temperature program for obtaining a $LiFePO_4$/C composite phase. The TG curve (Figure 1) shows three major mass loss steps. The first mass loss starting at 70 °C is associated with an endothermic peak in the DSC trace due to evaporation of ethanol. The surfactant and PMMA decomposed between 250 and 300 °C with endothermic DSC peaks at 263 and 294 °C. The third mass loss step between 300 and 425 °C is related to condensation of the walls and crystallization of $LiFePO_4$. According to the DSC data, the crystallization step occurred mainly in the temperature range from 400−425 °C, giving rise to an exotherm peaking at 409 °C. Removal of the surfactant and PMMA templates before this step would result in the loss of the supporting and confining scaffold for the inorganic phase, rendering grain growth during the crystallization process less controllable. It would therefore seem beneficial to treat the precursor first at temperatures below 250−300 °C to harden the inorganic skeleton, while it is still supported by the organic

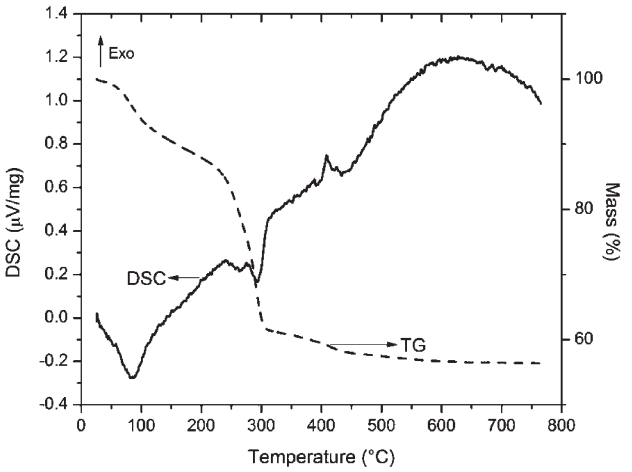

Figure 1. TG-DSC data for the cured $LiFePO_4$—PF-F127-PMMA composite obtained in a nitrogen atmosphere.

templates, and only then to treat the sample at higher temperatures (600−800 °C) to remove the templates and to induce further crystallization of the active $LiFePO_4$ phase. Contrary to our expectations, however, only powdered samples were obtained if the precursors were pretreated at 300 °C or below. Only precursors treated at temperatures higher than 325 °C formed monolithic samples. It appears that important factors for the formation of monolithic 3DOM/m $LiFePO_4$/C composites are the slow ramping rate causing slow removal of the template (PMMA and surfactant), and the 5 h treatment at an intermediate temperature right below the crystallization temperature, which strengthens the composite framework most effectively before the sample is heated above the crystallization temperature. On the basis of this information, all samples were aged first at 100 °C and then at 140 °C to enhance polymerization of the phenol formaldehyde phase. Pyrolysis was then carried out following programs with a lower temperature pretreatment step at 350 °C for 5 h and a higher temperature step at 600, 700, or 800 °C for 10 h.

Powder XRD was used to investigate the crystallinity and phase purity of the $LiFePO_4$/C composites. Figure 2 shows the wide-angle XRD patterns of samples pyrolyzed at different temperatures. In the temperature range from 600 to 800 °C, olivine $LiFePO_4$ was the only crystalline phase present. All of the sample peaks were indexed to the orthorhombic $LiFePO_4$ phase (*Pnmb*) with average lattice constants, a = 6.01 Å, b = 10.34 Å, c = 4.70 Å, and a unit-cell volume of 292 $Å^3$. A broad background peak between 18° and 32° 2θ, observed in all three patterns, originated from the nongraphitic carbon component. Other impurities such as FeP, Fe_3C, and Fe_2P, which are often found in $LiFePO_4$ samples formed in the presence of the reducing agent carbon, were not present or only present in such small quantities that they were undetectable by XRD. Such impurities are well-known for improving electronic conductivity but worsening rate performance of $LiFePO_4$.[47] Crystal sizes of $LiFePO_4$ in these samples were estimated by whole pattern fitting using Rietveld refinement. Because carbon was present as glassy carbon and therefore did not contribute any sharp peaks, all refinements were carried out for a single phase of $LiFePO_4$ using the *Pnmb* unit cell above. The calculated average crystallite sizes are summarized in Table 1. Crystallite sizes of $LiFePO_4$ in all three composite samples were small (≤68 nm), providing short

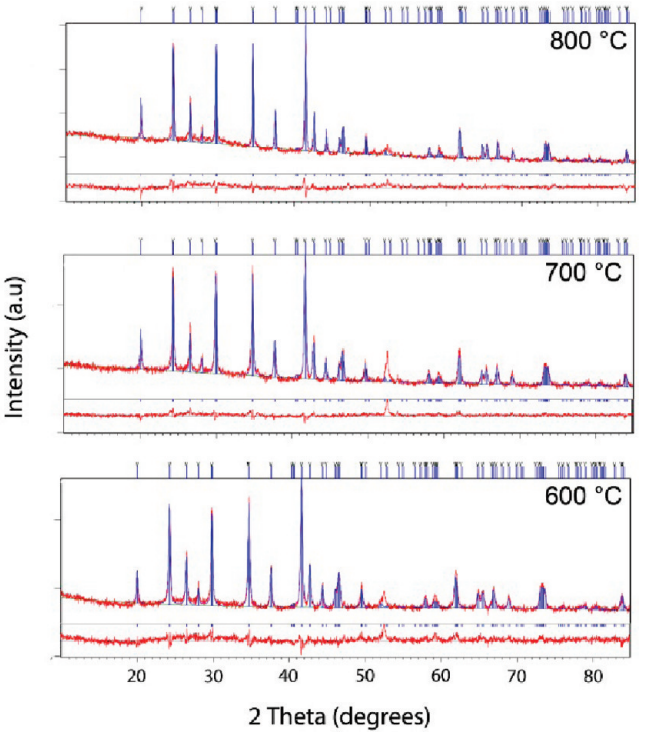

Figure 2. XRD patterns of $LiFePO_4$/C composites prepared by pyrolyzing precursors at 600, 700, and 800 °C for 10 h under nitrogen. The experimental patterns match the published line pattern for the olivine phase of $LiFePO_4$ (PDF # 00-40-1499, blue lines). Rietveld refinements are shown using a unit cell with *Pnmb* symmetry. The experimental patterns and difference patterns are shown in red, the calculated patterns in blue. The peak at 52.4° 2θ originates from the Al sample holder.

Table 1. Rietveld Refinement Data of Samples Pyrolyzed at 600, 700, and 800 °C

	temperature (°C)		
	600	700	800
a (Å)	6.0108(4)	6.0122(5)	6.0064(3)
b (Å)	10.3378(8)	10.3387(8)	10.3300(5)
c (Å)	4.6974(4)	4.6969(4)	4.6917(3)
unit-cell volume ($Å^3$)	291.9	292.0	291.1
crystallite size (nm)	41.9	47.6	68.2
R profile	3.56	3.3	3.23
weighted R profile	4.57	4.32	4.08
goodness of fit	1.68	1.94	2.08

diffusion paths for Li ions. They increased from 42 to 68 nm as the pyrolysis temperature increased from 600 to 800 °C. The small crystal sizes can be in part attributed to the isolation of particles by the carbon phase, as well as the PMMA spheres (before template combustion) or the macrovoid space (after combustion) which minimizes direct contact between particles and limits mass transport of the solid phase.

The carbon content of the 3DOM/m $LiFePO_4$/C composites was determined by TG-DSC analysis in air. For the sample synthesized at 600 °C, a mass loss of 30 wt % overlapped with a broad exothermic peak in the DSC trace (Figure 3A) between

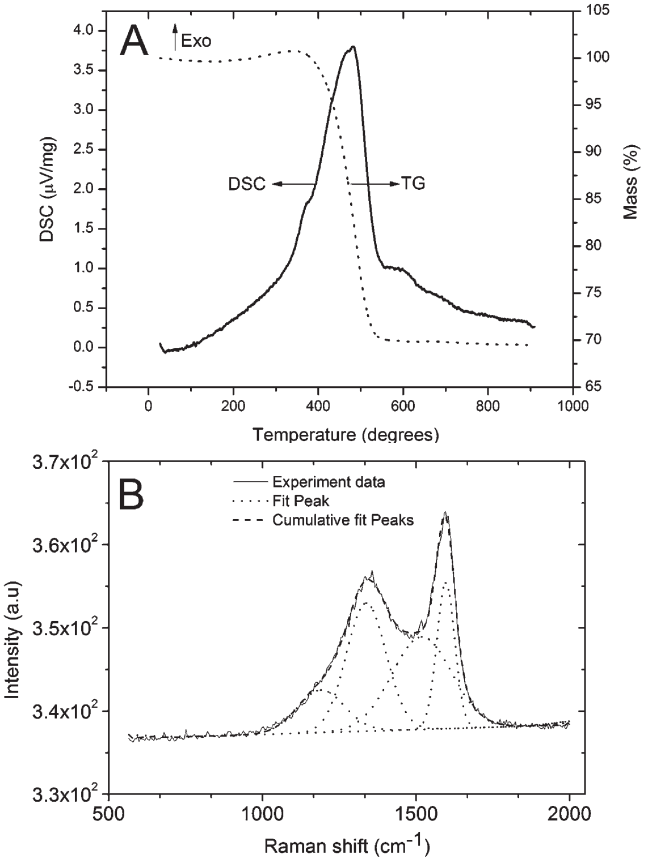

Figure 3. Information about the carbon component. (A) TG-DSC traces (obtained in air) and, (B) Raman spectrum of a 3DOM/m $LiFePO_4$/C composite pyrolyzed at 600 °C.

350 and 550 °C and corresponds to the carbon component in the composite. The carbon content was slightly lower for samples synthesized at 700 and 800 °C (27 and 22 wt %, respectively) (see Supporting Information, Figure S1), indicating that the carbon content was weakly affected by the pyrolysis temperature in this range. The carbon phase was further characterized by Raman spectroscopy. The Raman spectrum of 3DOM/m $LiFePO_4$/C shows two prominent peaks associated with sp^2 carbon (G-band, 1597 cm^{-1}) and sp^3 carbon (D-band, 1351 cm^{-1}) (Figure 3B). The G-band originates from the in-plane bond-stretching motion of pairs of sp^2 carbon atoms, while the D-band involves a breathing mode of A_{1g} symmetry, which is only active in the presence of disorder.[48] The G peak shifts from 1581 cm^{-1} in graphite to 1597 cm^{-1} in $LiFePO_4$/C composite, which indicates that carbon in the composite is nanocrystalline graphite. The size domain can be estimated using the equation $(I_D)/(I_G) = (C(\lambda))/(L_a)$, where I_D, I_G are the intensities of the disordered peak and the graphitic peak, respectively, $C(\lambda$ = 515.5 nm) = 4.4 nm, λ is the wavelength of the laser used in the Raman spectrometer, and L_a is the cluster diameter of nanocrystalline graphite.[48] The broad peaks contain additional contributions from sp^3 carbon sites present in amorphous carbonaceous materials.[49] Therefore simply fitting the spectrum with two peaks does not give an accurate value of I_D/I_G. To interpret the Raman features, the spectrum was instead deconvoluted with four Gaussian peaks situated at 1190, 1351, 1518, and 1597 cm^{-1}, where the additional bands at 1190 and 1518 cm^{-1} are associated with sp^3 carbon vibrations. On the

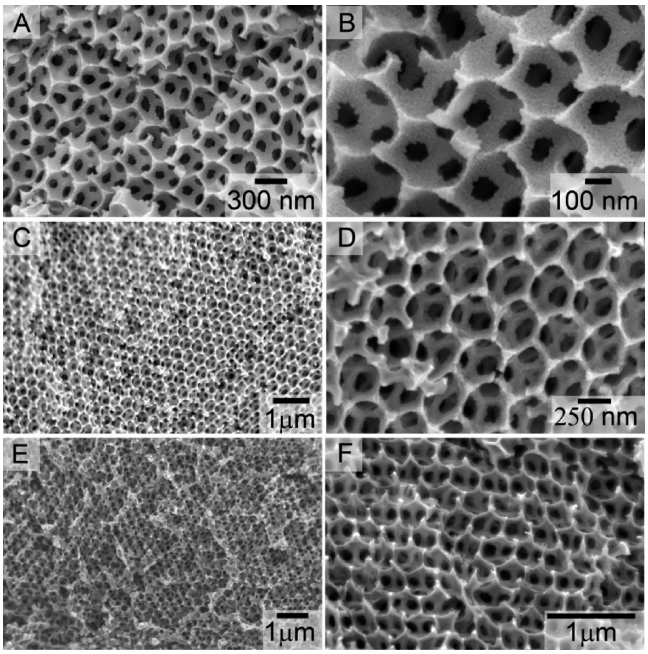

Figure 4. SEM images of samples pyrolyzed at 600 °C (A and B), 700 °C (C and D), and 800 °C (E and F) for 10 h under nitrogen.

basis of the fitted intensity ratios of the D and G peaks ($I_D/I_G \sim 0.88$), one can estimate the crystallite size in the direction of graphitic planes to be approximately 5 nm.[48,50]

The difference patterns from the Rietveld refinements (Figure 2) correspond mostly to the carbon phase. Judging from the low intensity and breadth of the peaks in the difference patterns, the extent of well-stacked graphitic layers perpendicular to the planes is also small. Similar features in Raman spectra and XRD patterns are typically observed for porous glassy carbon anode materials for lithium ion batteries made from resorcinol formaldehyde (RF) or phenol formaldehyde (PF) precursors.[51,52] Although the conductivity of such carbon materials is lower than that of graphite (ca. 0.1−0.3 S cm^{-1} for 3DOM/m carbon materials),[53] it is many orders of magnitude higher than that of $LiFePO_4$. The built-in carbon can enhance the electronic conductivity of the composite and help to improve rate performance of the cathode material.

The morphologies of the 3DOM/m $LiFePO_4$/C composites pyrolyzed at different temperatures were studied using field emission scanning electron microscopy (FE-SEM). Images A and B in Figure 4 show cross sections of a sample pyrolyzed at 600 °C. More than 90% of this sample has a well-ordered, interconnected macropore structure, in which the walls follow the curvature of the original colloidal crystal template. The texture of the wall provides a first indication of additional porosity (see below). The average macropore and window diameters of the sample pyrolyzed at 600 °C are 285 ± 10 nm and 90 ± 8 nm, respectively. As is typical for samples prepared from polymeric colloidal crystal templates, the macropore values are smaller than the diameters of the 400 nm PMMA templating spheres, due to shrinkage of the structure during thermal processing. The open, interconnected pore system in the 3DOM structure facilitates penetration of an electrolyte, and the large accessible surface of the material can enhance the exchange of Li^+ between the electrolyte and the electrode. The 3DOM structure is also well maintained for a sample pyrolyzed at

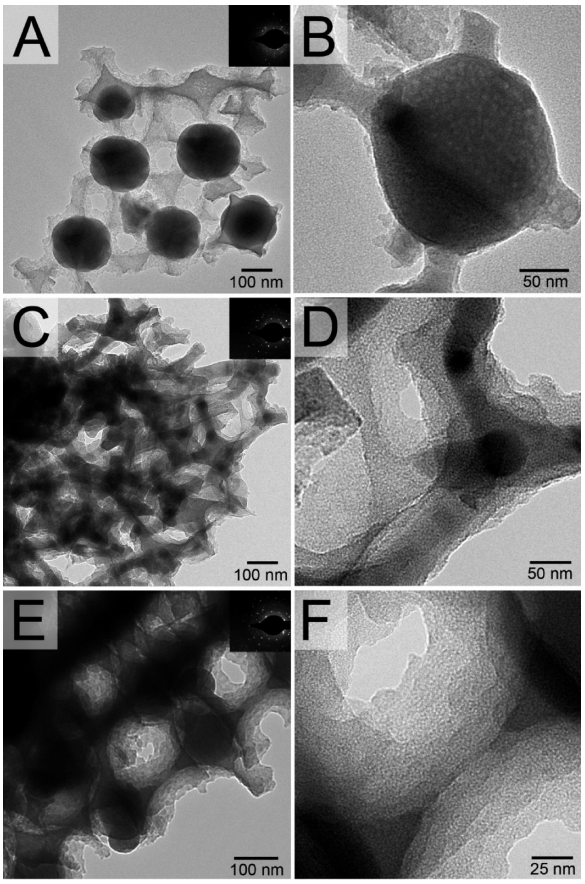

Figure 5. TEM images of 3DOM/m $LiFePO_4$/C samples pyrolyzed at 600 (A and B), 700 (C and D), and 800 °C (E and F). Insets in images (A), (C), and (E) are SAED patterns for the corresponding sample regions, confirming the crystalline nature of $LiFePO_4$ in the composites.

700 °C for 10 h. However, the walls are more strut-like, resulting in larger windows between interconnecting pores. After a higher temperature treatment at 800 °C for 10 h, a similar strut-like structure is observed. At this temperature, the 3DOM structure has undergone some distortion in a few regions, but an interconnected pore system is still preserved.

The morphologies of the 3DOM/m $LiFePO_4$/C composites were further analyzed by TEM. At lower magnifications, all samples showed features of the periodic macropore structure (Figure 5). The 3DOM structure is the inverse replica of the fcc colloidal crystal template. It can therefore be described as a network of interconnected octahedral and tetrahedral sites (replicas of the octahedral and tetrahedral holes in the close-packed template), with twice as many tetrahedral sites as octahedral sites. Interestingly, the curvature is different for the replicas of tetrahedral and octahedral sites in the materials pyrolyzed at 600 °C. Although in an ideal inverse opal structure both should be concave, in the 3DOM/m $LiFePO_4$/C materials only the tetrahedral regions are concave and the octahedral cubes are slightly convex, almost spherical. Furthermore, the octahedral replica sites appear significantly darker than the tetrahedral bridges. These features were observed for three different samples prepared at 600 °C in most areas of each sample (ca. 90%) (see also Supporting Information, Figure S2). In part, the contrast differences can be attributed to a greater thickness of the octahedral regions. However, another cause is likely to be an uneven distribution of $LiFePO_4$ in the composite phases. In TEM, the iron-rich regions would produce greater contrast than the carbon-rich phase with lower electron density. On the basis of the observed contrast differences and curvature differences, we propose that the octahedral sites are richer in $LiFePO_4$ (which is more prone to sintering than carbon), and the tetrahedral and thinner bridging regions are richer in carbon. Unfortunately, the resolution for elemental analysis in our TEM is insufficient to confirm this. Selected-area electron diffraction patterns (insets in Figure 5) show strong dot patterns characteristic of crystalline $LiFePO_4$, in agreement with XRD data, but they also represent the whole area viewed in the TEM image that contained both octahedral and tetrahedral replica units. The microphase separation is probably caused by a favorable crystallization energy for $LiFePO_4$ compared to the interaction energy that stabilizes the inorganic ($LiFePO_4$)−organic (carbon) interface. In terms of site preference, both $LiFePO_4$ and carbon should occupy octahedral sites (the bigger sites and lower surface-to-volume fraction) to lower their surface energy, but the contribution for the system from $LiFePO_4$ is greater because it is present in larger amounts (70 wt %). The structure of the sample pyrolyzed at 600 °C can therefore be described approximately as $LiFePO_4$-rich cubes that are interconnected through tetrahedral mesoporous carbon linkers. For samples treated at 700 and 800 °C, the features associated with partial phase separation of $LiFePO_4$ and carbon are still present but less pronounced (see Supporting Information, Figure S2). Fewer spherical components are observed in the TEM images, and the contrast is more uniform. At these higher temperatures, more efficient diffusion may overcome the surface energy differences.

This structure is especially interesting for high-power battery applications because it may offer several advantages over conventional carbon coatings. First, lithium diffusion paths are limited by the small crystallite size and the size of the octahedral replica features, in which the longest possible pathway is less than about 180 nm. Moreover, these sizes are tunable by altering the size of the PMMA template spheres. With conventional carbon coatings, $LiFePO_4$ particle growth is unrestricted, and typical particle sizes are a few micrometers, even if individual crystalline domains may be as small as a few tens of nanometers. If these continuous crystalline domains are correctly directed, that is, in the [010] direction, the diffusion path lengths double or triple, approaching the overall particle size. Finally, in the 3DOM/m composite, $LiFePO_4$ nanoparticles are efficiently wired by carbon, forming networks that are hundreds of micrometers in size.

The TEM images also show features that may be associated with micro- or mesoporosity. In the structural components linking tetrahedral replicas, disordered texture is visible, with spacings between about 1.5 and 4 nm. Larger circular features with sizes varying from 3 to 15 nm are visible in the darker octahedral replica regions of the sample pyrolyzed at 600 °C. The SAXS pattern for this sample shows a single weak peak at 0.4° 2θ corresponding to a spacing of 22 nm (Figure 6A) which may be associated with the bigger pores observed in the darker spherical regions (see Figure 5B and the Supporting Information, Figure S2). While a SAXS pattern of 3DOM/m C[18] synthesized from PF and F127 precursors shows two weak peaks between 0.7° and 3° 2θ, none of the SAXS patterns of $LiFePO_4$/C composites pyrolyzed at different temperatures showed any peaks in this range, consistent with the low degree of mesopore order observed by TEM (see Supporting Information, Figures S3 and S4).

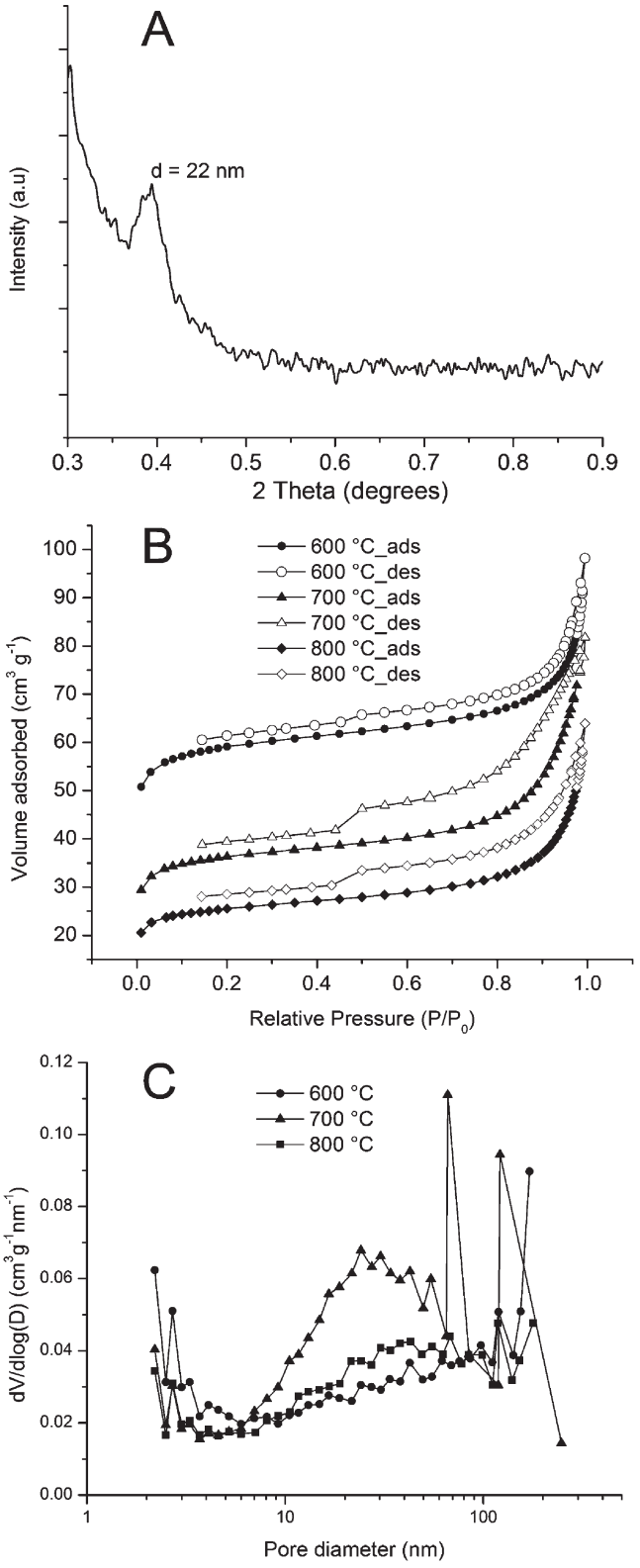

Figure 6. (A) SAXS pattern of 3DOM/m $LiFePO_4$/C treated at 600 °C, (B) Isotherms of 3DOM/m $LiFePO_4$/C samples pyrolyzed at 600, 700, and 800 °C, and (C) the corresponding pore size distributions.

The introduction of $LiFePO_4$ to the PF/F127 precursor mixture changed the interaction between the surfactant and the polymeric precursor, resulting in smaller and more disordered mesopores. To further examine the textural properties of the 3DOM/m $LiFePO_4$/C composites as a function of pyrolysis temperature, nitrogen adsorption−desorption measurements were performed. All isotherms feature a hysteresis loop between 0.5 and 0.95 P/P_0 typical for mesoporous structures (Figure 6B). However, the hysteresis loops are relatively narrow, characteristic for a pore size range near the border between mesopores (>2 nm) and micropores (<2 nm). Except for a small peak at 2.7 nm, the pore size distribution curves derived from the adsorption isotherms show no features that can be associated with templated mesopores (Figure 6C). In fact, for the sample pyrolyzed at 600 °C, which has the highest surface area (200 $m^2\ g^{-1}$, see Table 2), the largest fraction of this surface area and more than half of the pore volume is due to micropores. For samples pyrolyzed at higher temperatures, the surface areas decrease as high temperature treatment caused contraction, mainly of the micropores. Surface areas of 123 $m^2\ g^{-1}$ and 86 $m^2\ g^{-1}$ were obtained for samples pyrolyzed at 700 and 800 °C, respectively. In other dual templating syntheses of carbon-based materials with hierarchical porosity, mesopores tend to be larger even when the same surfactant (F127) is used. In a direct dual templating synthesis of 3DOM/m C uniform mesopores with diameters of 2.8 nm were formed,[52] and in a triconstituent synthesis of 3DOM/m C-SiO_2, mesopores were about 5.2 nm in diameter.[54] In the current synthesis, the additional inorganic precursor components appear to have prevented the formation of well-formed micellar arrays. However, the obtained surface areas were still much higher than those of nonporous analogues, which are typically in the range of a few $m^2\ g^{-1}$.

Electrochemical tests were carried out in a three-electrode cell on the sample pyrolyzed at 600 °C, because this sample exhibits the highest surface area, smallest crystallite size, yet high crystallinity, which are potentially useful features for high rate battery applications. Because of the monolithic nature of the electrode, no carbon black additive or binder were needed, which would lower the capacity of the cell. The cell was cycled at different rates from C/5 to 16C in the potential range between 2.0 and 4.2 V vs Li^+/Li. In this potential range, the contribution of carbon to lithium uptake is negligible.[53,55] At a slow rate (C/5), the discharge curve is characterized by a plateau at 3.39 V, which corresponds to the reaction $LiFePO_4 \rightarrow Li^+ + FePO_4 + e^-$. The electrode capacity is 150 mA h g^{-1} (based on the mass of $LiFePO_4$), which is 89% of the theoretical capacity. At higher rates, the capacity decreases but remains as high as 123 mA h g^{-1} at 1C, 103 mA h g^{-1} at 4C, 78 mA h g^{-1} at 8C, and 64 mA h g^{-1} at 16C rate (Figure 7). The good performance is attributed to the presence of the conductive carbon phase that embeds and connects the $LiFePO_4$ nanoparticles and to the high surface area of the composite that facilitates ionic transport across the interfaces. The electronic conductivity of the composite pyrolyzed at 600 °C is 0.14 S cm^{-1}, that is, much higher than that of bulk $LiFePO_4$ (10^{-9}−10^{-10} S cm^{-1}). In our tests, the monolithic $LiFePO_4$/C composite was able to support current densities as high as 2720 mA g^{-1} (at 16C rate, for a monolith containing 36.7 mg $LiFePO_4$ and a current of 100 mA).

Figure 8 shows the capacity of the cell cycled at different rates for the first 5 cycles at each rate. The cell capacity keeps stable, even at a rate as high as 16C, at which the cell is fully charged or discharged within 4 min. It is worth noting that as the current density is later reduced again to C/5, the capacity

Table 2. Dependence of Textural Properties of 3DOM/m $LiFePO_4$/C on Synthesis Temperature

pyrolysis temperature (°C)	BET surface area ($m^2\ g^{-1}$)	micropore area ($m^2\ g^{-1}$)	V_{pore} ($cm^3\ g^{-1}$)[a]	$V_{micropore}$ (%)	crystallite size (nm)[b]
600	200	157	0.13	55	41.9
700	123	90	0.12	36	47.6
800	86	61	0.08	34	68.2

[a] Single-point total pore volume at $P/P_0 = 0.983$. [b] Crystallite sizes for the $LiFePO_4$ phases in the composites were determined by Rietveld refinement of the powder XRD patterns.

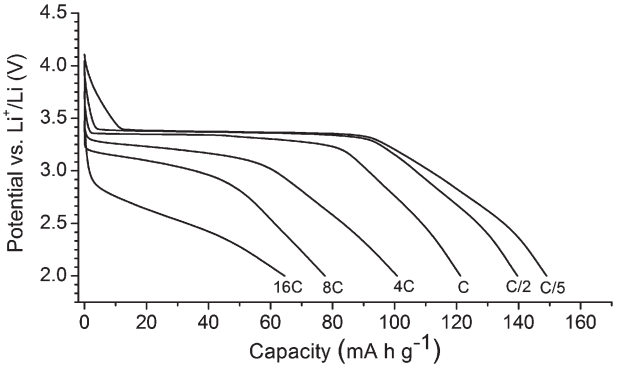

Figure 7. Discharge profile at different C rates for the 3DOM/m $LiFePO_4$/C composite sample pyrolyzed at 600 °C.

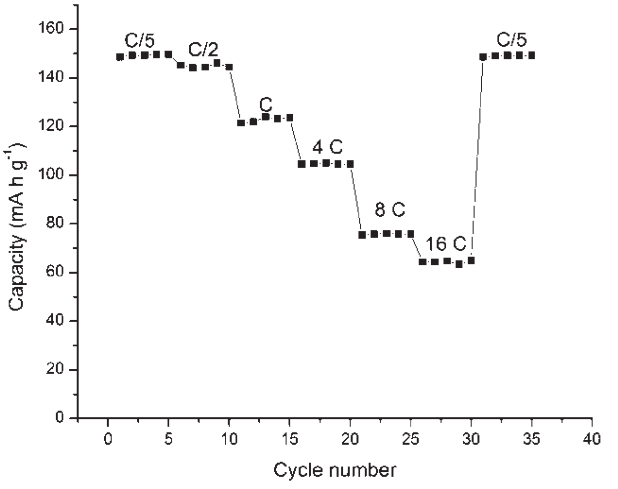

Figure 8. Capacity of the 3DOM/m $LiFePO_4$/C composite sample pyrolyzed at 600 °C and cycled for 5 cycles each at different rates.

returns to its original value, which indicates that the electrode material remained stable. This stability is attributed to the interconnected macropore system that assists mass transport and the built-in carbon component which improves the mechanical stability of the composite. Both features give the composite the stability to withstand the stresses caused by the phase change from $LiFePO_4$ to $FePO_4$, and by the infiltration of electrolyte into the composite.

The composite was cycled at a rate of 4C over 70 cycles and at 8C over 100 cycles to test the capacity retention at high rates (Figure 9). The data demonstrate the excellent capacity retention at both rates with Coulombic efficiencies near 99%.

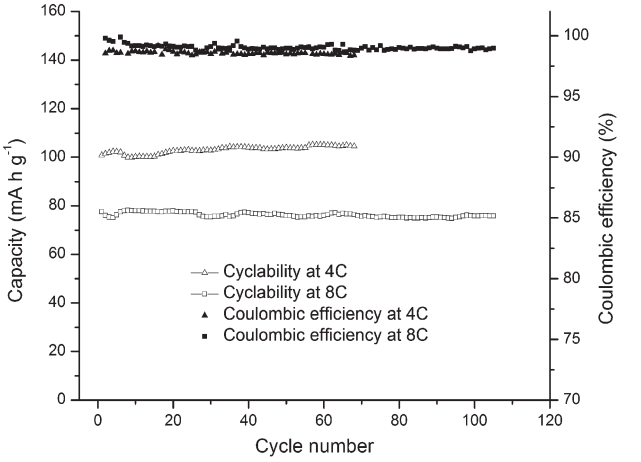

Figure 9. Capacity retention and Coulombic efficiency of $LiFePO_4$/C composite pyrolyzed at 600 °C when cycled at 4C and 8C rates.

CONCLUSION

The combination of colloidal crystal templating with surfactant templating provides an efficient synthetic method for forming $LiFePO_4$/C composites with high capacities for lithiation (150 mA h g^{-1} at C/5, 78 mA h g^{-1} at 8C, and 64 mA h g^{-1} at 16C rate) and excellent capacity retention at high rates. The colloidal crystal templating approach maintains small particle sizes and easy access for electrolyte and lithium ions to the active cathode phase through an interconnected macropore system. Although the secondary pore structure introduced by the surfactant template was not as well-defined as in related dual templating syntheses of pure 3DOM/m C or mixed 3DOM/m C-SiO_2 materials, the additional micropores and small mesopores provided the composites with surface areas as high as 200 $m^2\ g^{-1}$. Another role of the surfactant was to act as a compatibilizer for the complex precursor mixture.

In composite samples pyrolyzed at 600 °C, carbon and $LiFePO_4$ selectively occupy different locations in the inverse opal structure. The resulting structure can therefore be described as a network of cubic $LiFePO_4$-rich nanoparticles wired together by tetrapodal mesoporous carbon-rich particles. This special structure gives the electrode greater structural stability so that millimeter-sized monolithic porous electrodes could be formed, and it provides improved conductivity to support high currents. The materials are therefore of interest as cathodes for high-rate lithium-ion batteries. Although the macropore space contributes to nonactive volume, such volume may be utilized to accommodate additional active material, for example in a 3D-interpenetrating, nanostructured battery.[51,56] The concepts of micro phase-separation and site preference found for the 3DOM/m $LiFePO_4$/C composite may also apply to other templated electrode systems containing multiple components, in which

active material may be embedded and wired together in an electronically more conductive phase.

■ ASSOCIATED CONTENT

Supporting Information. TG-DSC traces, TEM images, and SAXS patterns of 3DOM/m $LiFePO_4$/C composites pyrolyzed at various temperatures. This material is available free of charge via the Internet at http://pubs.acs.org.

■ AUTHOR INFORMATION

Corresponding Author
*E-mail: a-stein@umn.edu. Phone: 1-612-624-1802.

■ ACKNOWLEDGMENT

This research was supported partially by the Office of Naval Research (Grant N00014-07-1-0608) and the National Science Foundation (DMR-0704312). Portions of this work were carried out in the University of Minnesota Characterization Facility, which receives partial support from the NSF through the MRSEC, ERC, MRI and NNIN programs. The authors thank Prof. Bill Smyrl for access to the electrochemical facilities.

■ REFERENCES

(1) Padhi, A. K.; Nanjundaswamy, K. S.; Goodenough, J. B. *J. Electrochem. Soc.* **1997**, *144*, 1188–1194.
(2) Tarascon, J.-M.; Armand, M. *Nature* **2001**, *414*, 359–367.
(3) Manthiram, A. *J. Phys. Chem. Lett.* **2011**, 176–184.
(4) Nishimura, S.-I.; Kobayashi, G.; Ohoyama, K.; Kanno, R.; Yashima, M.; Yamada, A. *Nat. Mater.* **2008**, *7*, 707–711.
(5) Huggins, R. A. *Advanced Batteries*; Springer: New York, 2009.
(6) Chung, S.-Y.; Bloking, J. T.; Chiang, Y.-M. *Nat. Mater.* **2002**, *1*, 123–128.
(7) Meethong, N.; Kao, Y.-H.; Speakman, S. A.; Chiang, Y.-M. *Adv. Funct. Mater.* **2009**, *19*, 1060–1070.
(8) Kang, B.; Ceder, G. *Nature* **2009**, *458*, 190–193.
(9) Hu, Y.-S.; Guo, Y.-G.; Dominko, R.; Gaberscek, M.; Jamnik, J.; Maier, J. *Adv. Mater.* **2007**, *19*, 1963–1966.
(10) Huang, H.; Yin, S. C.; Nazar, L. F. *Electrochem. Solid-State Lett.* **2001**, *4*, A170–A172.
(11) Konarova, M.; Taniguchi, I. *Mater. Res. Bull.* **2008**, *43*, 3305–3317.
(12) Murugan, A. V.; Muraliganth, T.; Ferreira, P. J.; Manthiram, A. *Inorg. Chem.* **2009**, *48*, 946–952.
(13) Kim, M. G.; Cho, J. *Adv. Funct. Mater.* **2009**, *19*, 1497–1514.
(14) Muraliganth, T.; Murugan, A. V.; Manthiram, A. *J. Mater. Chem.* **2008**, *18*, 5661–5668.
(15) Gaberscek, M.; Kuzma, M.; Jamnik, J. *Phys. Chem. Chem. Phys.* **2007**, *9*, 1815–1820.
(16) Long, J. W.; Sassin, M. B.; Fischer, A. E.; Rolison, D. R.; Mansour, A. N.; Johnson, V. S.; Stallworth, P. E.; Greenbaum, S. G. *J. Phys. Chem. C* **2009**, *113*, 17595–17598.
(17) Baxter, J.; Bian, Z.; Chen, G.; Danielson, D.; Dresselhaus, M. S.; Fedorov, A. G.; Fisher, T. S.; Jones, C. W.; Maginn, E.; Kortshagen, U.; Manthiram, A.; Nozik, A.; Rolison, D. R.; Sands, T.; Shi, L.; Sholl, D.; Wu, Y. *Energy Environ. Sci.* **2009**, *2*, 559–588.
(18) Wang, Z.; Kiesel, E. R.; Stein, A. *J. Mater. Chem.* **2008**, *18*, 2194–2200.
(19) Wang, Z.; Fierke, M. A.; Stein, A. *J. Electrochem. Soc.* **2008**, *155* (9), A658–A663.
(20) Woo, S.-W.; Dokko, K.; Nakano, H.; Kanamura, K. *J. Mater. Chem.* **2008**, *18*, 1674–1680.
(21) Su, F.; Zeng, J.; Bai, P.; Lv, L.; Guo, P.-Z.; Sun, H.; Li, H. L.; Yu, J.; Lee, J. Y.; Zhao, X. S. *Ind. Eng. Chem. Res.* **2007**, *46*, 9097–9102.
(22) Lu, A.-H.; Schmidt, W.; Spliethoff, B.; Schuth, F. *Adv. Mater.* **2003**, *15*, 1602–1606.
(23) Fan, J.; Wang, T.; Yu, C.; Tu, B.; Jiang, Z.; Zhao, D. *Adv. Mater.* **2004**, *16*, 1432–1436.
(24) Zhang, W.-M.; Hu, J.-S.; Guo, Y.-G.; Zheng, S.-F.; Zhong, L.-S.; Song, W.-G.; Wan, L.-J. *Adv. Mater.* **2008**, *20*, 1160–1165.
(25) Wang, Z.; Ergang, N. S.; Al-Daous, M. A.; Stein, A. *Chem. Mater.* **2005**, *17*, 6805–6813.
(26) Cao, F. F.; Wu, X. L.; Xin, S.; Guo, Y. G.; Wan, L. J. *J. Phys. Chem. C* **2010**, *114*, 10308–10313.
(27) Tirado, J. L.; Santamaría, R.; Ortiz, G. F.; Menéndez, R.; Lavela, P.; Jiménez-Mateos, J. M.; Gómez García, F. J.; Concheso, A.; Alcántara, R. *Carbon* **2007**, *45*, 1396–1409.
(28) Monnier, A.; Schuth, F.; Huo, Q.; Kumar, D.; Margolese, D.; Maxwell, R. S.; Stucky, G. D.; Krishnamurty, M.; Petroff, P.; Firouzi, A.; Janicke, M.; Chmelka, B. F. *Science* **1993**, *261*, 1299–1303.
(29) Yang, P.; Zhao, D.; Margolese, D. I.; Chmelka, B. F.; Stucky, G. D. *Chem. Mater.* **1999**, *11*, 2813–2826.
(30) Yang, P.; Zhao, D.; Margolese, D. I.; Chmelka, B. F.; Stucky, G. D. *Nature* **1998**, *396*, 152–155.
(31) Dominko, R.; Bele, M.; Goupil, J.-M.; Gaberscek, M.; Hanzel, D.; Arcon, I.; Jamnik, J. *Chem. Mater.* **2007**, *19*, 2960–2969.
(32) Lim, S.; Yoon, C. S.; Cho, J. *Chem. Mater.* **2008**, *20*, 4560–4564.
(33) Luo, J.-Y.; Wang, Y.-G.; Xiong, H.-M.; Xia, Y.-Y. *Chem. Mater.* **2007**, *19*, 4791–4795.
(34) Doherty, C. M.; Caruso, R. A.; Smarsly, B. M.; Drummond, C. J. *Chem. Mater.* **2009**, *21*, 2895–2903.
(35) Doherty, C. M.; Caruso, R. A.; Drummond, C. J. *Energy Environ. Sci.* **2010**, *3*, 813–823.
(36) Wang, G.; Liu, H.; Liu, J.; Qiao, S.; Lu, G. M.; Munro, P.; Ahn, H. *Adv. Mater.* **2010**, *22*, 4944–4948.
(37) Doherty, C. M.; Caruso, R. A.; Smarsly, B. M.; Adelhelm, P.; Drummond, C. J. *Chem. Mater.* **2009**, *21*, 5300–5306.
(38) Liu, R.; Shi, Y.; Wan, Y.; Meng, Y.; Zhang, F.; Gu, D.; Chen, Z.; Tu, B.; Zhao, D. *J. Am. Chem. Soc.* **2006**, *128*, 11652–11662.
(39) Kang, Y.-S.; Lee, H. I.; Zhang, Y.; Han, Y. J.; Yie, J. E.; Stucky, G. D.; Kim, J. M. *Chem. Commun.* **2004**, 1524–1525.
(40) Li, F.; Wang, Z.; Ergang, N. S.; Fyfe, C. A.; Stein, A. *Langmuir* **2007**, *23*, 3996–4004.
(41) Meng, Y.; Gu, D.; Zhang, F.; Shi, Y.; Yang, H.; Li, Z.; Yu, C.; Tu, B.; Zhao, D. *Angew. Chem., Int. Ed.* **2005**, *44*, 7053–7059.
(42) Schroden, R. C.; Al-Daous, M.; Sokolov, S.; Melde, B. J.; Lytle, J. C.; Stein, A.; Carbajo, M. C.; Fernández, J. T.; Rodríguez, E. E. *J. Mater. Chem.* **2002**, *12*, 3261–3267.
(43) Van Der Pauw, L. J. *Philips Tech. Rev.* **1958/59**, *20*, 220–224.
(44) Ellis, B. L.; Makahnouk, W. R. M.; Makimura, Y.; Toghill, K.; Nazar, L. F. *Nat. Mater.* **2007**, *6*, 749–753.
(45) Dong, A.; Ren, N.; Tang, Y.; Wang, Y.; Zhang, Y.; Hua, W.; Gao, Z. *J. Am. Chem. Soc.* **2003**, *125*, 4976–4977.
(46) Li, D.; Zhou, H.; Honma, I. *Nat. Mater.* **2004**, *3*, 65–72.
(47) Song, M.-S.; Kim, D.-Y.; Kang, Y.-M.; Kim, Y.-I.; Lee, J.-Y.; Kwon, H.-S. *J. Power Sources* **2008**, *180*, 546–552.
(48) Ferrari, A. C.; Robertson, J. *Phys. Rev. B* **2000**, *61*, 14095–14107.
(49) Doeff, M. M.; Hu, Y.; McLarnon, F.; Kostecki, R. *Electrochem. Solid-State Lett.* **2003**, *6*, A207–A209.
(50) Tuinstra, F.; Koenig, J. L. *J. Chem. Phys.* **1970**, *53*, 1126–1130.
(51) Ergang, N. S.; Fierke, M. A.; Wang, Z.; Smyrl, W. H.; Stein, A. *J. Electrochem. Soc.* **2007**, *154*, A1135–A1139.
(52) Wang, Z.; Li, F.; Ergang, N. S.; Stein, A. *Chem. Mater.* **2006**, *18*, 5543–5553.
(53) Wang, Z.; Li, F.; Ergang, N. S.; Stein, A. *ECS Trans.* **2008**, *6*, 199–204.
(54) Wang, Z.; Stein, A. *Chem. Mater.* **2008**, *20*, 1029–1040.
(55) Dahn, J. R. *Phys. Rev. B* **1991**, *44*, 9170–9177.
(56) Ergang, N. S.; Lytle, J. C.; Lee, K. T.; Oh, S. M.; Smyrl, W. H.; Stein, A. *Adv. Mater.* **2006**, *18*, 1750–1753.